On Statistical Methods Beyond Correlation in Coherence Analysis Based on Ultrasound

Mahshid Dodel, Raphaël Dumas, Adrian Basarab, François Varray
INSA-Lyon, Université Claude Bernard Lyon 1, CNRS, Inserm, CREATIS UMR 5220, U1294, France

***Abstract*—This paper investigates statistical methods for analyzing the spatial coherence function to estimate myocardial fiber orientation, a critical factor in understanding cardiac microstructure and advancing cardiac imaging diagnostics. Four approaches, namely Correlation, Mutual Information, Kraskov Mutual Information, and Granger Causality, were evaluated using an *in vitro* experimental dataset designed to simulate myocardial fiber alignment. Our findings reveal that Granger Causality effectively captures complex and highly anisotropic structures, such as corners, while mutual information-based methods demonstrate superior stability and consistency across simpler regions. By applying a filter based on fractional anisotropy, the performance of each method was refined, highlighting their distinct strengths in fiber tracking. To leverage these complementary advantages, we propose the Fused and Consensus methods, which integrate the strengths of individual approaches to enhance coherence analysis and improve fiber orientation estimation. This study shows that the four methods complement each other by excelling in different aspects of fiber tracking, offering a robust framework for accurately characterizing fiber orientation. These insights can potentially improve the assessment of myocardial microstructure and aid in the early diagnosis and treatment of cardiac diseases.**

***Index Terms*—Fiber tracking, Ultrasound coherence imaging, Fractional Anisotropy, Granger Causality, Mutual Information**

I. Introduction

Cardiovascular diseases are the leading cause of death in Europe, claiming over 3 million lives each year, and highlight the urgent need for advances in cardiac microstructure analysis [1]. The structure of myocardial fibers plays a critical role in cardiac function, influencing both the mechanical and electrical properties of the heart [2]. Accurate mapping of these fibers is essential for understanding the complex dynamics of cardiac function and early diagnosing of various cardiac pathologies.

Current myocardial fiber imaging techniques, such as magnetic resonance diffusion tensor imaging (MR-DTI), provide detailed structural information but have significant limitations, including long acquisition times, high cost, limited frame rates, and sensitivity to tissue motion. Given these limitations, Ultrasound (US) imaging is a promising alternative due to its portability, cost-effectiveness, and faster acquisition times. It offers real-time, non-invasive visualization of internal structures. By emitting high-frequency sound waves and processing their echoes, the US generates tomographic images without radiation exposure [3]. These characteristics make the US a strong candidate for cardiac imaging, particularly for assessing myocardial fiber orientation.

In the literature, three ways of extracting fiber orientation have been described using US imaging: (i) the backscatter coefficient, which evaluates the spectral characteristic to provide insight into tissue microstructure [4], [5], (ii) shear wave elastography, where the shear wave velocity evolves along the local fiber orientation [6], and (iii) spatial coherence, where the coherence of signals received by transducer elements characterizes the local anisotropy [7].

Among these methods, spatial coherence, namely backscatter tensor imaging (BTI), stands out for its ability to provide high-resolution visualization of myocardial fibers [7]. In 3D BTI, spatial coherence is measured using a 2D matrix probe, and the complete 3D anisotropy is estimated [8]. This technique has been applied to composite materials and biological tissues, such as the myocardium, to determine fiber orientation. In medical imaging, a significant limitation of these works is the combination of a large number of transducer elements with limited time samples, making it difficult to find similarities between signals.

Correlation-based coherence analysis captures only linear relationships, missing non-linear and causal interactions [9]. The standard approach, which relies on sample covariance or cross-correlation between RF signals, fails to fully characterize complex dependencies. To address these limitations, our study introduces Mutual Information (MI) and Granger Causality (GC) as alternatives [10]. MI captures both linear and non-linear relationships, while GC uncovers causal interactions, offering directional insights into tissue behavior. GC has been applied in contexts such as electrograms in atrial fibrillation studies to identify causal influences from latent forces on signals [11]. Replacing the traditional covariance matrix with matrices derived from MI and GC improves the accuracy and robustness of fiber orientation estimation, particularly in noisy and complex environments. Integrating these methods through fused and consensus strategies leverages their complementary strengths, advancing coherence analysis for fiber tracking.

II. Background on BTI

The methodology used in this research employs a plane wave coherent compounding technique [7] that improves US image quality. The process begins with the successive emission of multiple tilted plane waves. The backscattered echoes from these waves are combined to create voxel-specific focal zones. Note that this focalization step is mandatory with the spatial coherence theory of [12]. The coherence of the signals received by different pairs of transducer elements is then

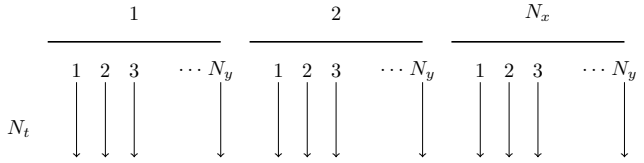

Fig. 1: The diagram illustrates the probe structure, with arrows indicating how the signals are mapped into the matrix $\mathbf{S}$.

calculated. By analyzing the coherence of the signals, it is possible to extract the local orientation of the tissues at each focalized voxel by fitting an ellipse to the coherence map [7] or using the principal component analysis (PCA) to find the primary direction [8].

A. Spatial coherence calculation for each voxel

The 2D matrix representing the US probe is structured as an array with N_x elements along the x-axis and N_y elements along the y-axis. The layout of the probe elements can be expressed as

$$\begin{pmatrix} (1,1) & (1,2) & \cdots & (1,N_y) \\ (2,1) & (2,2) & \cdots & (2,N_y) \\ \vdots & \vdots & \ddots & \vdots \\ (N_x,1) & (N_x,2) & \cdots & (N_x,N_y) \end{pmatrix}. \tag{1}$$

Each element (i,j) in this array corresponds to a specific position on the probe, where $i \in [1,N_x]$ and $j \in [1,N_y]$.

Let $\mathbf{s}_n \in \mathbb{R}^{1\times N_t}$ represent the signal for one element, where $n = 1,2,\ldots,N_xN_y$ denotes one of the $N_x \times N_y$ elements forming the probe, and N_t is the number of time samples considered locally around the focalized voxel. The temporal signals collected from all the elements are regrouped in a 2D data matrix $\mathbf{S} \in \mathbf{R}^{N_t\times(N_x\times N_y)}$, following the configuration shown in Fig. 1.

The matrix $\mathbf{S}$, which contains the Radio Frequency (RF) signals, is normalized to obtain $\hat{\mathbf{S}}$. This is achieved by individually normalizing each RF signal in $\mathbf{S}$: subtracting its mean $\mu_{\mathbf{S}}$ and dividing by its standard deviation $\sigma_{\mathbf{S}}$ along the time axis.

From the normalized signal matrix $\hat{\mathbf{S}}$, the sample covariance matrix $\mathbf{\Sigma_S}$ is then calculated as follows:

$$\mathbf{\Sigma_S} = \frac{1}{N_t-1} \times \hat{\mathbf{S}} \times \hat{\mathbf{S}}^T \in \mathbb{R}^{(N_x\times N_y)\times(N_x\times N_y)}. \tag{2}$$

Here, $\hat{\mathbf{S}}^T$ denotes the transpose of $\hat{\mathbf{S}}$, which swaps its rows and columns.

B. Coherence Function Calculation

The 2D coherence function $\mathbf{R}$ is computed using a matrix formulation that improves computational efficiency for matrix US probes [8]. It involves normalizing the coherence over the total number of time points N_t by averaging the coherence function at each time step. For each time step, the focused, normalized signals are used to compute a 2D spatial correlation between signals at different locations (x,y) and their shifted counterparts $(x+\Delta x, y+\Delta y)$. This correlation is then normalized using a spatial shift-based denominator that accounts for the number of elements involved in the computation. The coherence is computed for all possible spatial offsets $(\Delta x, \Delta y)$ and averaged over time. One can show that the coherence function can be computed from the covariance matrix by taking the average of thoroughly chosen terms:

$$\begin{aligned} \mathbf{R}(\Delta x,\Delta y) = \frac{1}{\mathbf{card}(\Psi_{\Delta x,\Delta y})} \sum_i \sum_j \mathbf{\Sigma_S}(i,j) \\ \text{s.t.} \quad \left\lceil \frac{i}{N_y} \right\rceil - \left\lceil \frac{j}{N_y} \right\rceil = \Delta x \\ (i \mod N_y) - (j \mod N_y) = \Delta y, \end{aligned} \tag{3}$$

where $\mathbf{card}(\Psi_{\Delta x,\Delta y})$ is the number of elements extracted from $\mathbf{\Sigma_S}$ for a given pair $(\Delta x,\Delta y)$, and $\lceil\cdot\rceil$ stands for the round toward infinity operator. Note that in (3) Δx and Δy take values from 1 to N_x, respectively from 1 to N_y. This results in a coherence map $\mathbf{R}$ of size $N_x \times N_y$. This approach evaluates the linear similarity between RF signals from different transducer elements, making it ideal for large datasets in US imaging. It helps assess spatial coherence by measuring how strongly signals from different positions are related, revealing information about fiber orientation.

C. Angle estimation

PCA is used in this study to extract the primary angles from the coherence function map. PCA reduces the dimensionality of the coherence data by transforming it into a set of orthogonal components, with the first principal component capturing the maximum variance in the data. This approach simplifies the analysis while preserving the most essential information for angle estimation [8].

The main output of this analysis is the assessment of tissue anisotropy, which is quantified using the Fractional Anisotropy (FA) metric. FA measures the deviation from isotropy, where values close to zero indicate uniformity in all directions, i.e., isotropy, and values closer to one signify significant anisotropy, reflecting a directional preference in the tissue structure [13]. By analyzing the principal components from PCA, FA captures the degree of directional variation within the tissue, allowing for a more precise understanding of fiber orientation and the relationship between tissue structure and its anisotropic properties [8].

III. Statistical Methods for Coherence Analysis

As mentioned in section II, statistical methods are critical for analyzing spatial coherence functions in US imaging to estimate local fiber orientation. This section outlines the application of two advanced techniques, Mutual Information (MI) and Granger Causality (GC), and their role in improving the accuracy and robustness of fiber orientation estimation. The main idea is to replace the covariance matrix in (2) with matrices constructed from MI or GC values between pairs of RF signals. The coherence map computation follows the same process but uses MI or GC coefficients instead of correlation values. In the following, the principles of MI and GC are summarized.

A. Mutual Information: Capturing Non-linear Dependencies

MI measures how much information is shared between two signals, indicating how knowledge of one signal reduces uncertainty about the other [14]. This makes MI particularly useful for detecting complex interactions.

For two signals $\mathbf{s}_n$ and $\mathbf{s}_m$ of $\mathbf{S}$, the MI between them is defined as:

$$I(m,n) = \sum_{x \in s_m} \sum_{y \in s_n} p(x,y) \log \left(\frac{p(x,y)}{p(x)p(y)} \right), \quad (4)$$

where $p(\mathbf{s}_m, \mathbf{s}_n)$ represents the joint probability distribution of the signals at positions m and n, while $p(\mathbf{s}_m)$ and $p(\mathbf{s}_n)$ are the marginal probability distributions for signals $\mathbf{s}_m$ and $\mathbf{s}_n$, respectively.

Rooted in information theory, MI measures the amount of shared information between two signals by calculating how much knowledge of one signal reduces uncertainty about the other. This is based on entropy, a concept that quantifies the unpredictability or randomness of a variable [10].

Calculating MI directly from probability distributions can be computationally demanding, especially for large datasets. Two estimation approaches are commonly used to meet this challenge. The first classical method relies on histograms or kernel density estimation to approximate joint and marginal distributions, but it can be slow when dealing with large data [14]. The Kraskov method's second approach uses nearest-neighbor distances to estimate the MI, significantly reducing computational complexity. This makes it more efficient and robust, especially for smaller sample sizes, by avoiding the need to estimate probability distributions fully.

B. Granger Causality: Uncovering Causal Relationships in Fiber Orientation

GC measures the directional influence between two signals, determining whether one signal can predict another [15]. Unlike correlation and MI, which capture statistical dependencies but not directionality, GC provides insight into causal relationships.

A key property of GC is that while correlation and MI produce a symmetric dependence matrix, the Granger Causality Index (GCI) forms an asymmetric matrix, reflecting the directional influence between signals.

In the bivariate GC model, the signal value $\mathbf{s}_n[k]$ is predicted using both its past values and the past values of another signal $\mathbf{s}_m[k]$. The autoregressive (AR) model for $\mathbf{s}_n$ without the influence of $\mathbf{s}_m$ is:

$$\mathbf{s}_n[k] = \sum_{i=1}^{p} a_i \mathbf{s}_n[k-i] + \epsilon_n[k], \quad (5)$$

where a_i are the autoregressive model coefficients for the past values of $\mathbf{s}_n$, p is the number of time lags, and $\epsilon_n[k]$ is the residual error. When the past values of $\mathbf{s}_m[k]$ are included in the model, we have:

$$\mathbf{s}_n[k] = \sum_{i=1}^{p} a_i \mathbf{s}_n[k-i] + \sum_{i=1}^{p} b_i \mathbf{s}_m[k-i] + \epsilon'_n[k], \quad (6)$$

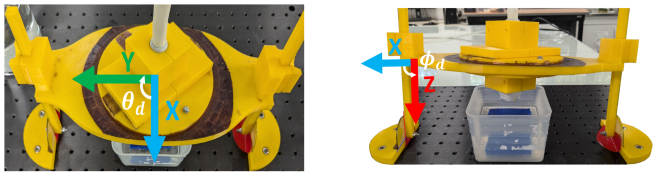

(a) Top view (b) Front view

Fig. 2: Top (a) and front (b) views of the *in vitro* setup for fiber orientation measurements.

where b_i are the coefficients for the past values of $\mathbf{s}_m$, and $\epsilon'_n[k]$ is the new residual error after incorporating $\mathbf{s}_m[k]$.

The GC is established if the inclusion of the past values of $\mathbf{s}_m[k]$ (i.e., the b_i terms) significantly reduces the prediction error for $\mathbf{s}_n[k]$. The GCI is then computed as:

$$\text{GCI}(m \to n) = \log \left(\frac{\text{var}(\epsilon_n[k])}{\text{var}(\epsilon'_n[k])} \right). \quad (7)$$

If $\text{GCI}(m \to n) > 0$, then $\mathbf{s}_m$ Granger-causes $\mathbf{s}_n$, indicating a directional causal relationship.

C. Complementary Maps

To capitalize on the advantages of each approach, two combined methods were proposed: the **Fused Map** and the **Consensus Map**. The fused map, derived by averaging the normalized values of coherence, GC, and MI metrics, provides a smooth and balanced representation of fiber orientation. The consensus map refines results by thresholding each metric at the top 40% (greater than 0.6) and summing the binary outputs to highlight regions of strong agreement across methods. This threshold was selected based on visual and quantitative evaluations.

IV. Materials and Results

A. Data Acquisition and Preprocessing

An *in vitro* setup was created by wrapping 0.1 mm nylon thread around a disk to simulate an oriented muscle sheet [8]. The final dimensions of the sheet were 40×45 mm, larger than the aperture of a 1024-element Vermon matrix array probe (3.47 MHz, 0.3 mm pitch, 10.5×9.6 mm footprint). The disk was placed on a rotary platform to control the in-plane angle θ_d, calibrating to minimize out-of-plane motion ($\phi_d \approx 0°$). Pictures of the experimental setup are shown in Fig. 2. A Verasonic Vantage 256 US system was used for the US acquisition, transmitting 25 plane waves from -20° to 20°. Due to multiplexing, only 256 elements were used, with the transmission divided into four synthetic sub-apertures. The received signals were beam-formed using plane-wave compounding. To simulate different orientations, acquisitions were made at different nylon thread angles $\theta_d = \{-60°, -45°, -30°, 0°, 30°, 45°, 60°\}$. Computations for each method were performed at a consistent depth of 37 mm.

B. Results

Fig. 3 shows the estimated fiber angles for each method at a ground truth angle of 60°, with an interpolation factor of 2 for visualization. Correlation estimated the angle at

TABLE I: Mean and standard deviation of fiber angle estimates for all methods at various ground truth angles.

Theta	$\mu \pm \sigma$ Correlation	$\mu \pm \sigma$ GC	$\mu \pm \sigma$ MI Classic	$\mu \pm \sigma$ MI Kraskov	$\mu \pm \sigma$ Fused	$\mu \pm \sigma$ Consensus
-60	-57.4 ± 4.2	-60.9 ± 5.8	-55.4 ± 3.3	-56.8 ± 4.9	-58.4 ± 3.4	-56.8 ± 10.2
-45	-40.8 ± 6.9	-44.5 ± 9.6	-41.3 ± 5.4	-41.1 ± 7.3	-42.6 ± 4.2	-42.5 ± 6.1
-30	-29.0 ± 4.9	-32.7 ± 4.3	-32.0 ± 4.9	-28.3 ± 6.7	-31.1 ± 2.4	-28.5 ± 5.7
0	-0.4 ± 3.9	-0.5 ± 0.8	-0.3 ± 2.0	-0.1 ± 2.5	-0.4 ± 0.9	-0.1 ± 1.6
30	24.4 ± 5.9	29.0 ± 6.0	26.8 ± 6.3	24.5 ± 7.2	27.4 ± 2.7	22.9 ± 5.8
45	38.6 ± 8.4	45.4 ± 7.9	41.2 ± 6.2	39.0 ± 8.1	42.5 ± 4.2	41.4 ± 6.6
60	58.7 ± 5.7	60.0 ± 8.4	56.7 ± 5.5	58.4 ± 6.2	60.1 ± 3.3	59.7 ± 7.1

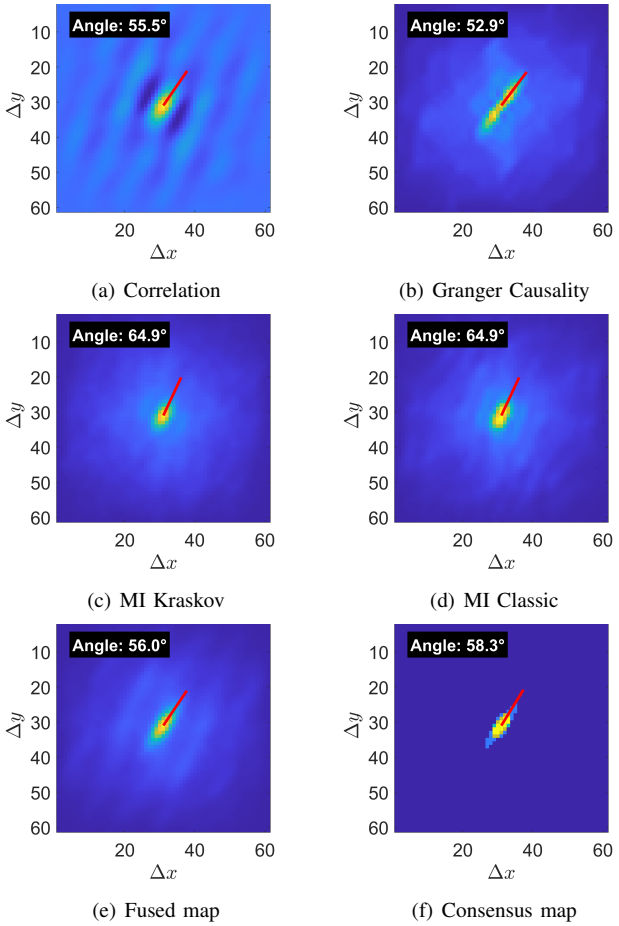

(a) Correlation (b) Granger Causality

(c) MI Kraskov (d) MI Classic

(e) Fused map (f) Consensus map

Fig. 3: Estimated fiber angles for the coherence maps for a ground truth angle of 60° obtained with (a) Correlation: 55.5°, (b) Granger Causality: 52.9°, (c) MI Kraskov: 64.9°, (d) MI Classic: 64.9°, (e) Fused map: 56.0°, and (f) Consensus map: 58.3°.

55.5°, relatively close to the ground truth, though with a less sharp orientation. GC estimated 52.9°, further from the true value, but its larger ellipse suggests it may be better for complex scenarios by capturing causal relationships. Both the Kraskov and classical MI methods estimated 64.9°, closely matching the true value and effectively capturing non-linear dependencies with consistent results. The Fused map estimated 56.0°, integrating multiple estimations for enhanced accuracy, while the Consensus map provided an estimation of 58.3°, balancing the strengths of all methods.

Table I compares the mean and standard deviation over a range of ground truth angles for the six approaches. By applying a filter based on FA thresholding, considering $FA > 0.3$ for Correlation, MI Classic and MI Kraskov, and $FA > 0.45$ for GC due to its tendency to capture higher anisotropy regions, the performance of each method was further refined. For the MI methods, the shape of the estimated ellipses tended to be more circular, indicating less anisotropy in the data. In contrast, GC resulted in more elongated, linear ellipses, indicating higher anisotropy. While GC provided means closer to the ground truth in several cases, it also had higher standard deviations, indicating more significant variability. The MI methods performed better with lower standard deviations, making them more consistent and stable across different angles. Therefore, although GC may provide more accurate mean estimates, the MI methods are more reliable overall due to their lower variability.

For fused and consensus approaches, a lower FA threshold of $FA > 0.2$ was applied for these two maps. This choice was made to prevent excessive fiber elimination, as a stricter threshold of $FA > 0.3$ would have removed a significant number of fibers. However, it was observed that the lower FA threshold did not significantly affect the mean and standard deviation values, suggesting that the inclusion of lower FA regions still maintained consistency in the results. These approaches reinforce how the individual strengths of Correlation, GC, and MI-based methods can be leveraged together for improved robustness and accuracy.

Fig. 4 shows the fiber tracking results for the four different approaches. It highlights how GC could detect and track fibers even at the region's edges, whereas the other three methods struggled to detect an orientation. This suggests that these methods can complement rather than replace each other. Each method excels in different aspects: while GC performs better at capturing complex structures such as corners, the MI and correlation methods provide more stable results in less complex regions. In addition, Fig. 4(e-f) further demonstrates how these methods can be combined to improve coherence analysis. Indeed, the Fused and Consensus maps enhance this by integrating their complementary strengths, improving coherence analysis in US imaging.

V. Discussion

The results highlight the complementary strengths of Correlation, MI, and GC for fiber orientation estimation in US coherence imaging. GC effectively captures highly anisotropic structures, such as corners, due to its ability to model causal dependencies. However, its higher standard deviation suggests increased variability, particularly in simpler regions. In contrast, MI-based methods demonstrate more stable and consistent performance, especially in uniform areas with dominant non-linear dependencies. The fused and consensus maps integrate these complementary strengths, improving overall robustness.

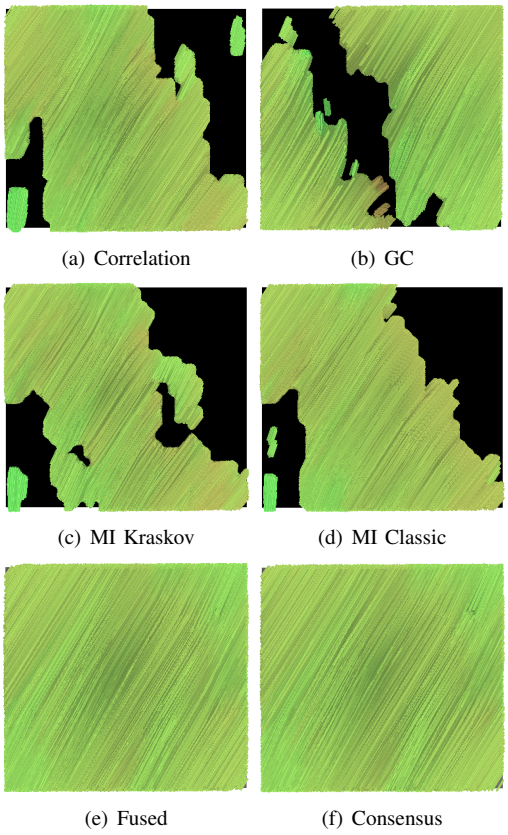

(a) Correlation (b) GC

(c) MI Kraskov (d) MI Classic

(e) Fused (f) Consensus

Fig. 4: Fiber tracking results at a 60° ground truth angle using (a) Correlation, (b) GC, (c) MI Kraskov, (d) MI Classic, (e) Fused, and (f) Consensus.

While this study provides a detailed analysis of coherence-based fiber tracking methods, some limitations should be considered. First, the computational cost of MI and GC is higher than correlation-based approaches. The Kraskov MI method relies on nearest-neighbor estimation, and GC requires autoregressive modeling, making them computationally intensive. To evaluate their feasibility, we benchmarked execution time on a representative RF block. Correlation completed in approximately 0.06 s, MI Kraskov in 0.85 s, MI Classic in 2.51 s, and Granger Causality in 1.00 s. These results highlight the trade-off between speed and robustness, motivating future GPU or parallel optimization for real-time use.

Another limitation is that the evaluation was performed on an *in vitro* experimental model. This setup allows for a controlled assessment of different methods, ensuring a well-defined ground truth for fiber orientation. However, real-world variability in cardiac tissue structures may influence the performance of these approaches.Future work will focus on validating the methods first on *ex vivo* biological tissues, then on *in vivo* ultrasound acquisitions, to assess their robustness and clinical applicability.

Finally, as shown in Fig. 4, the visualization-based comparison of these methods indicates that GC is more sensitive to structural anisotropy, whereas MI-based approaches provide higher stability. The fused and consensus maps improve the accuracy by leveraging the strengths of each method, making them promising tools for fiber tracking in medical imaging.

VI. Compliance with Ethical Standards

This is a numerical study on data acquired on phantoms, for which no ethical approval was required.

Acknowledgment

This work was supported by the LABEX PRIMES (ANR-11-LABX-0063) and LABEX CELYA (ANR-10-LABX-0060) of the Université de Lyon, within the program "Investissements d'Avenir" (ANR-11-IDEX-0007), operated by the French National Research Agency (ANR), the GDR IASIS, and the ANR DETLA project ANR-24-CE45-7060. This material is based upon work done on the ISO 9001:2015 PILoT facility. The RF Verasonics generator was cofounded by the FEDER program, Saint-Etienne Metropole (SME), and Conseil General de la Loire (CG42) within the framework of the SonoCardio-Protection Project leaded by Pr Pierre Croisille.

References

[1] A. Timmis, V. Aboyans, P. Vardas, N. Townsend, A. Torbica, M. Kavousi, G. Boriani, R. Huculeci, D. Kazakiewicz, D. Scherr *et al.*, "European society of cardiology: the 2023 atlas of cardiovascular disease statistics," *European Heart Journal*, vol. 45, no. 38, pp. 4019–4062, 2024.

[2] J. Cleutjens, "The infarcted myocardium Simply dead tissue, or a lively target for therapeutic interventions," *Cardiovascular Research*, vol. 44, no. 2, pp. 232–241, 1999.

[3] V. Chan and A. Perlas, "Basics of ultrasound imaging," *Atlas of ultrasound-guided procedures in interventional pain management*, pp. 13–19, 2011.

[4] Y. Song, C. M. Kube, J. Zhang, and X. Li, "Higher-order spatial correlation coefficients of ultrasonic backscattering signals using partial cross-correlation analysis," *The Journal of the Acoustical Society of America*, vol. 147, no. 2, pp. 757–768, 2020.

[5] M. Yang, T. M. Krueger, M. R. Holland, and J. G. Miller, "Anisotropy of the backscatter coefficient of formalin-fixed ovine myocardium," *The Journal of the Acoustical Society of America*, vol. 122, no. 1, pp. 581–586, 2007.

[6] W.-N. Lee, M. Pernot, M. Couade, E. Messas, P. Bruneval, A. Bel, A. A. Hagege, M. Fink, and M. Tanter, "Mapping Myocardial Fiber Orientation Using Echocardiography-Based Shear Wave Imaging," *IEEE Transactions on Medical Imaging*, vol. 31, no. 3, pp. 554–562, 2012.

[7] C. Papadacci, V. Finel, J. Provost, O. Villemain, P. Bruneval, J.-L. Gennisson, M. Tanter, M. Fink, and M. Pernot, "Imaging the dynamics of cardiac fiber orientation in vivo using 3D Ultrasound Backscatter Tensor Imaging," *Scientific Reports*, vol. 7, no. 1, p. 830, 2017.

[8] R. Dumas, B. Pialot, and F. Varray, "Complete 3D anisotropy measurement with coherence imaging," in *IEEE International Ultrasonics Symposium (IUS)*, 2023, pp. 1–4.

[9] A. Papana, "Connectivity Analysis for Multivariate Time Series: Correlation vs. Causality," *Entropy*, vol. 23, no. 12, p. 1570, 2021.

[10] N. N. Taleb, "Fooled by Correlation: Common Misinterpretations in Social "Science"," 2019.

[11] D. Luengo and V. Elvira, "Latent Variable Analysis of Causal Interactions in Atrial Fibrillation Electrograms," in *Computing in Cardiology Conference (CinC)*, 2016.

[12] A. Derode and M. Fink, "Spatial coherence of ultrasonic speckle in composites," *IEEE Transactions on ultrasonics, ferroelectrics, and frequency control*, vol. 40, no. 6, pp. 666–675, 1993.

[13] C. Papadacci, M. Tanter, M. Pernot, and M. Fink, "Ultrasound backscatter tensor imaging (BTI)," *IEEE Transactions on Ultrasonics, Ferroelectrics, and Frequency Control*, vol. 61, no. 6, pp. 986–996, 2014.

[14] T. M. Cover and J. A. Thomas, *Elements of information theory*, ser. Wiley series in telecommunications. New York: Wiley, 1991.

[15] L. Barnett and A. K. Seth, "The MVGC multivariate Granger causality toolbox: A new approach to Granger-causal inference," *Journal of Neuroscience Methods*, vol. 223, pp. 50–68, 2014.